DOI: 10.1109/TASC.2021.3065882
FERMILAB-PUB-21-567-TD
(accepted)

Magnetic and Mechanical Analysis of a Large Aperture 15 T Cable Test Facility Dipole Magnet

Giorgio Vallone, Diego Arbelaez, Douglas Martins Araujo, Amalia Ballarino, Paolo Ferracin, Aurelio Hafalia, Simon Hopkins, Vittorio Marinozzi, Ian Pong, Soren Prestemon, GianLuca Sabbi, Gueorgui Velev

***Abstract*—The US Department of Energy (DOE) Office of Science (SC), is funding a large bore "Cable Test Facility Magnet" for testing advanced cables and inserts in high transverse field. This is a joint effort between the Office of High Energy Physics (HEP) and the Office of Fusion Energy Sciences (FES). The background field magnet for this facility is being developed at Lawrence Berkeley National Laboratory (LBNL) while the cryostat and test facility will be located and operated by Fermi National Accelerator Laboratory (FNAL). The Nb_3Sn dipole magnet, which will provide the transverse background field, is designed to generate a field of 15 T in a 100 x 150 mm bore at 1.9 K. The conceptual design of a block-type dipole with flared ends and a structure based on key-and-bladder technology will be introduced. The results of the magnetic and mechanical analysis will be presented.**

***Index Terms*—Dipoles, Nb_3Sn, test facilities.**

I. INTRODUCTION

The ability to test high current cables in a high background magnetic field is of strong interest for fusion and high energy physics (HEP) applications. The EDIPO test facility provided such a capability with a background field of up to 12.4 T [1], until irreparable damage occurred to the EDIPO magnet. As a joint effort between the offices of Fusion Energy Sciences and High Energy Physics, the US Department of Energy has recently decided to fund a high field cable test facility for testing advanced cables and inserts in a high transverse magnetic field. A background field magnet for this facility is being developed at Lawrence Berkeley National Laboratory (LBNL) while the cryostat and test facility will be designed, constructed, and operated by Fermi National Laboratory (FNAL) [2]. The magnet will provide a background field of 15 T in a 100 x 150 mm bore operating at 1.9 K.

A block coil design with flared ends using a shell based key-and-bladder structure has been chosen. This builds on the extensive experience gained at LBNL through the design, fabrication, and test of the HD magnet series, which achieved a bore field of 13.8 T with a 36 mm bore [3], [4]; and of the FRESCA2 magnet at CERN, which achieved a bore field of 14.6 T in circular 100 mm bore [5], [6]. Magnetic and mechanical analyses for magnets with similar field strength targets and bore dimensions have been previously done for the LD1 magnet at LBNL [7] and the recent HEPDIPO studies [8]–[10]. In this paper, we describe the test facility dipole magnet design features, and the magnetic and mechanical analysis for 16 T bore field operation.

This work was supported by the US Department of Energy Offices of Science, High Energy Physics (HEP), and Fusion Energy Sciences.

G. Vallone, D. Arbelaez, P. Ferracin, A. Hafalia, I. Pong, S. Prestemon and G. Sabbi are with the Lawrence Berkeley National Laboratory, Berkeley, CA 94720 USA (e-mail: gvallone@lbl.gov).

V. Marinozzi and G. Velev are with the Fermi National Accelerator Laboratory, Batavia, IL 60510, USA.

D. Martins Araujo, A. Ballarino and S. Hopkins are with CERN, CH-1211 Geneva, Switzerland.

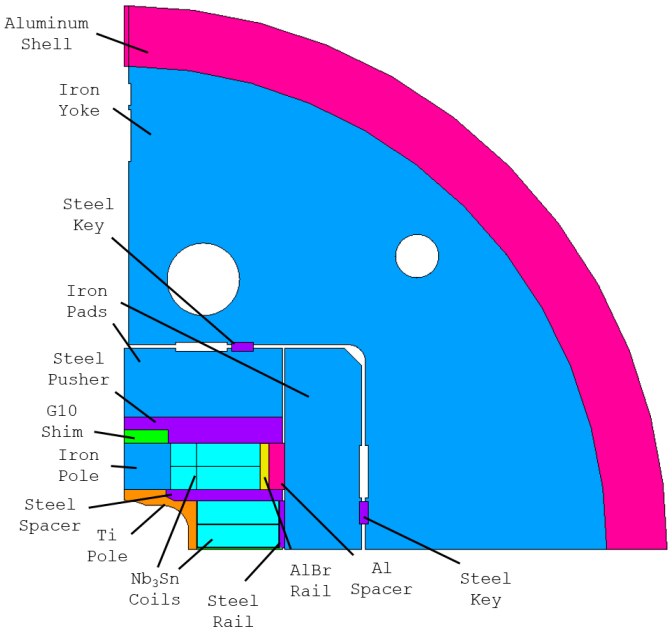

Fig. 1. A diagram of the shell based, key-and-bladder magnet structure cross section. The main features include the coils, poles, Al shell, iron pads, keys, and various spacers. The geometry and materials used for the spacers and rails are optimized to minimize the stress in the coils and structure.

II. MAGNET DESCRIPTION

The test facility dipole (TFD) is designed with a rectangular aperture of 94 mm × 144 mm with a superimposed round profile with 100 mm diameter for compatibility with FRESCA2 samples. A 3 mm test well wall thickness is assumed, leading to a 100 mm × 150 mm magnet aperture. The magnet is specified to produce a background field of 15 T, but a design target of 16 T has been set to provide margin and potential for higher field operation.

The mechanical structure is shown in the cross-section of Fig. 1. The inner coil is wound around a titanium pole, the outer coil around an iron pole. The coils are separated by a 13 mm thick stainless steel spacer. The coils are loaded vertically by a steel pusher and an iron pad. The steel pusher has a slot that allows for the insertion of a G10 shim. This

solution allows the reduction of the vertical load on the titanium pole caused by the iron forces. An alternative would be to leave a gap, but this would cause a local increase of stress on the iron pole top surface. The horizontal load is applied by an iron pad that loads the rails. The outer coil uses an aluminum bronze rail and aluminium spacer instead of a classic stainless steel one. This solution significantly reduces the stresses in the outer coil. The design employs the bladder and key technology [11] to apply the prestress at room temperature. The bladders and the keys are inserted between the pads and the iron yoke, and in between the vertical surface of the yoke. The iron yoke is surrounded by an aluminum shell, which provides a further increase of prestress during the cooldown to cryogenic temperature, thanks to the differential contraction with respect to the rest of the magnet.

A. Alternative Layouts

In the initial phase of the design, a graded coil layout, where a thinner cable (with smaller diameter wire) is used in the lower field regions, was considered. Previous analysis for this approach was performed as part of the HEPDIPO collaboration [8]. This approach has several advantages since it leads to a more compact and efficient magnetic design. However, the added risk due to the need for development of additional joints between the cable segments was deemed too high for this project. Therefore, a non-graded coil design is being pursued.

For the non-graded design, two different configurations are being considered. The first layout has the outer surface of coils shifted relative to one another (LD style [7]). For the second layout, the coils are aligned with each other on their outer surface (FRESCA2 style). Fig. 2 shows a diagram of the two layouts. In sections IV and V results from the magnetic and mechanical analysis for both layouts are shown. The layouts are constrained to have the same number of total turns and to produce similar field quality for comparison purposes. Ultimately, the LD style has been chosen for the baseline design since better mechanical performance could be achieved with this layout.

III. Parameters and Design Constraints

Magnet design criteria were defined in order to consistently evaluate the acceptability and performance of different designs. The criteria include material limits, prestress requirements, and design performance indexes. The material limits are defined starting from the MQXF design criteria [12], which follows a graded approach to evaluate the serviceability of the structure. We consider as fragile all materials with a K_I lower than $100\,\mathrm{MPa\,m^{1/2}}$, such as aluminum [13], magnetic steels [14], and titanium [15]. Assumed material limits are provided in Table I, where σ_m is the maximum stress allowable, with a safety factor of 1.2. The stress limit has to be compared with the Von Mises equivalent stress for ductile materials, and with the highest between Von Mises and the first principal stress for fragile ones.

Debonding between the winding and the rest of the coil is considered a possible cause of training [16], [17]. In order to control this effect, we limit the tension at the winding pole/winding interface, as computed in a bonded FE model, to $20\,\mathrm{MPa}$. Possible spikes of the tension at the corner coils are neglected, up to a length of $1\,\mathrm{mm}$.

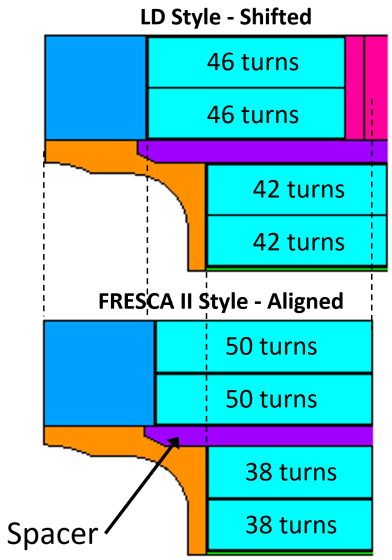

Fig. 2. Two different non-graded coil layouts are considered in the design study. The top one (LD style) has the outer surface of the coils shifted relative to one another. The bottom one (FRESCA2 style) has the outer surface of the coils aligned to one another.

TABLE I
Assumed Material Limits

Material	Ref.	Details	σ_m, R.T.	σ_m, 4.5 K
Titanium	[15]	Grade V	692	813
Al. Bronze	[18]	C61400	342	473
Aluminum	[13]	A7075	400	343
Magnetic Steel	[14]	Armco	175	364
Stainless Steel	[19]	SS316LN	198	508
Stainless Steel	[19]	Nitronic 40	568	1189
		Parallel to the fibers	214	413
G10	[19]	Normal, tension	17	17
		Normal, compression	350	624

The design performance is evaluated on the basis of the load line margin, the maximum coil stress in the high and low field regions, and the field quality for consistent comparison of different options.

IV. Magnetic Analysis

In this section, the magnetic calculations and the margin analysis are presented. For the margin analysis, two different conductor parametrizations are used. The first parametrization (A) corresponds to a conductor that was recently procured by CERN from Bruker OST targeting high J_c for CERN's high field magnet programme. The second parametrization (B) corresponds to the MQXF conductor, scaled to a diameter of 1.1 mm [20]. For both parametrizations, the parameter values are established using data from transport current measurements on existing wires at 4.2 K.

For the margin analysis, the non-Cu critical current density is assumed to follow the scaling law:

$$j_c = \frac{C_o}{B}\left(1-t^{1.5}\right)^{\alpha}\left(1-t^{2}\right)^{\alpha} b^{0.5}\left(1-b\right)^{2} \qquad (1)$$

TABLE II
STRAND PARAMETERS

Parameter	Value - A †	Value - B ‡
Wire Diameter [mm]	1.1	1.1
Cu to non-Cu ratio	0.9	1.17
Wire Architecture	RRP 162/169	RRP 108/127
C_0 [AT/mm^2]	235520	222800
α	1.0	1.0
T_{C0*} [K]	17.0	17.0
B_{C20*} [T]	30.0	29.3
Cabling Degradation [%]	5	5

† FCC development wire.
‡ Values scaled from the 0.85 mm HL-LHC MQXF wire to a 1.1 mm diameter.

TABLE III
CABLE PARAMETERS

Parameter	Value
Number of Strands	44
Cable Width †	26.2 mm
Cable Thickness †	1.95 mm
Insulation Thickness	0.15 mm

† After heat treatment.

where t is the normalized temperature, $t = T/T_{C0}$, B is the magnetic field, b is the normalized field, $b = B/B_{C2}$, and $B_{C2} = B_{C20}\left(1 - t^{1.52}\right)$. Table II shows the wire parameters for both type A and type B conductors. A conservative assumption of 5% cabling degradation is used for both conductors.

Table III shows the assumed after heat treatment cable parameters for the magnetic and mechanical analysis. The dimensions include a post-reaction expansion factor. A cable development effort is currently under way. The type A conductor is preferred due to the higher transport current. A quench protection analysis performed using STEAM-LEDET demonstrates that this magnet can be safely protected within the assumed quench protection constraints. The details of this analysis can be found in [2].

Figure 3 shows the magnet load line and critical current curves (current per strand) for the test facility dipole magnet. Both conductors, type A (FCC Dev. Wire) and B (HiLumi 1.1), are shown in this plot. For the chosen coil layout (LD style) the operational margin, I_{op}/I_{ss}, for a 16 T bore field at 1.9 K is 81.2% for type A conductor and 85.7% for type B conductor. Figure 4 shows the magnetic field strength distribution in both coils for the LD style layout. The peak magnetic field occurs in coil 1 and has a value of 16.5 T.

TABLE IV
ALTERNATIVE LAYOUT RESULTS

Parameter	Shifted	Aligned
Operating Current	15.6 kA	15.5 kA
Short Sample Current	19.2 kA	19.1 kA
Load Line Margin	81.2%	81.0%
Max Field (coil 1)	16.5 T	16.5 T
Max Field (coil 2)	16.1 T	16.0 T
Stored Energy (per quadrant)	1.8 MJ/m	1.8 MJ/m
Total Fx (inner)	6.3 MN/m	6.3 MN/m
Total Fy (inner)	-2.7 MN/m	-1.8 MN/m
Total Fx (outer)	10.0 MN/m	9.6 MN/m
Total Fy (outer)	-6.9 MN/m	-7.6 MN/m

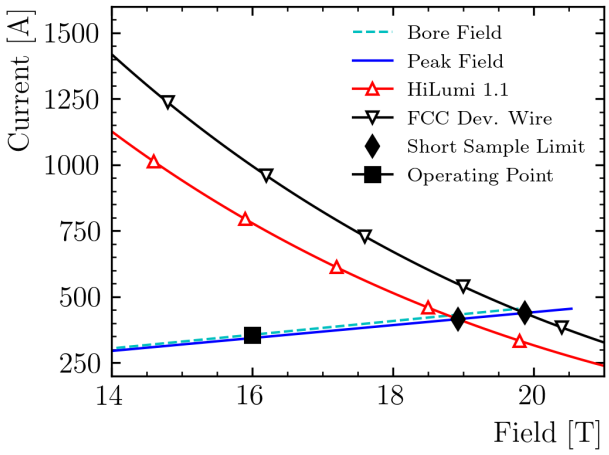

Fig. 3. Magnetic load line for the test facility dipole magnet operating at 1.9 K. The critical current curve for the wire with both type A and type B conductors are shown. The diamond markers represent the short sample limit for each conductor, while the square marker represents the operating current for 16 T bore field.

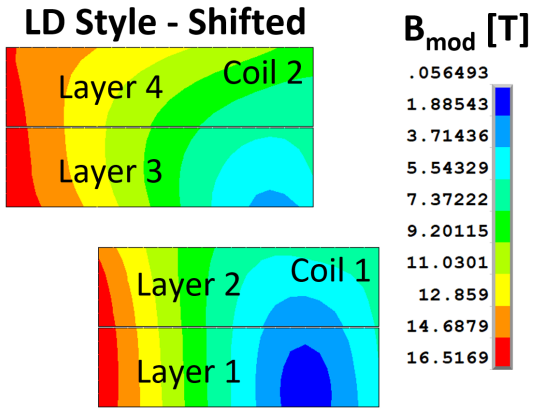

Fig. 4. Magnetic field strength distribution on the coil cross-sections for 16 T operation for the shifted layout. The peak magnetic field occurs on coil 1 with a maximum value of 16.5 T.

While the field quality is not a critical optimization parameter for a background field test facility magnet, it is important to maintain some reasonable restrictions for fair comparison between different designs. For both design layouts, the location and dimensions of the coils were chosen to keep the field variation within a 50 mm radius below approximately ±0.25%. Figure 5 shows the field deviation range at 16 T nominal bore field for a reference radius of 30, 40, and 50 mm. The maximum field deviation is ±0.23%, ±0.08%, ±0.03%, at a reference radius of 50 mm, 40 mm, and 30 mm respectively.

Table IV shows the results of the magnetic analysis for both layouts. A similar operating current is required for 16 T operation with similar operating margin. The main differences between the two layouts are in the distribution of the vertical forces between the coils. The shifted design has a higher vertical force on coil 1 and a lower force on coil 2. In the next section, the mechanical analysis will be presented which leads to the shifted layout being chosen as the baseline design.

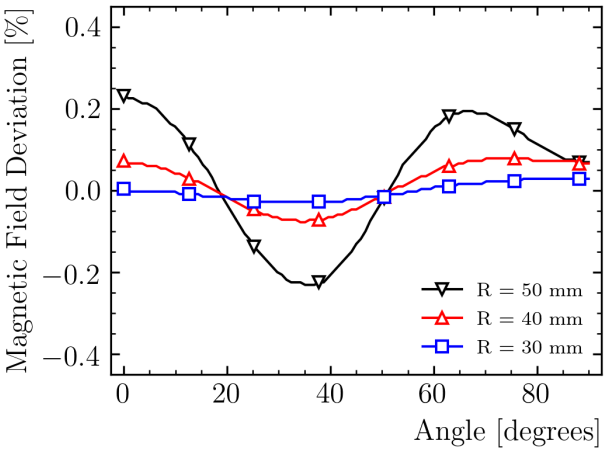

Fig. 5. Variation from the baseline magnetic field as a function of angle at 16 T operation for the shifted layout. The maximum field deviation is ±0.23%, ±0.08%, ±0.03%, at a reference radius of 50 mm, 40 mm, and 30 mm respectively.

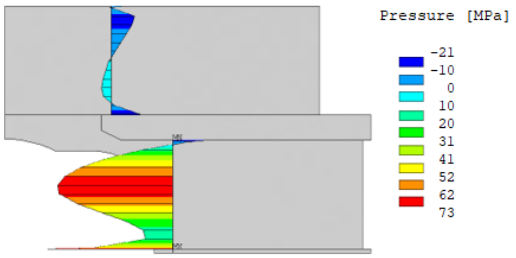

Fig. 6. Contact pressure at the coil/pole interface, in 15 Pa. The maximum tension, excluding 1 element at every corner (0.5 mm width), is equal to 15 MPa on the outer layer.

V. Mechanical Analysis

A. 2D Mechanical Analysis

The mechanical design for each of the two coil layouts was optimized with an iterative process. Each variation of the design was run against the criteria defined in Section III. The results presented here were obtained from 2D simulations in ANSYS APDL. Comparison with 3D FE models shows that, at least in the central cross-section of the magnet, the 2D results are reliable.

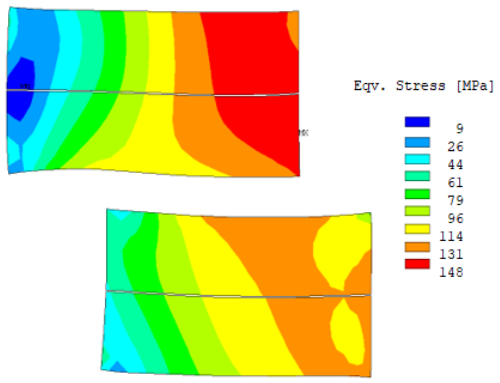

Fig. 7. Von Mises equivalent stress, in Pa, on the superconducting coil at 16 T. The maximum stress is equal to 166 MPa.

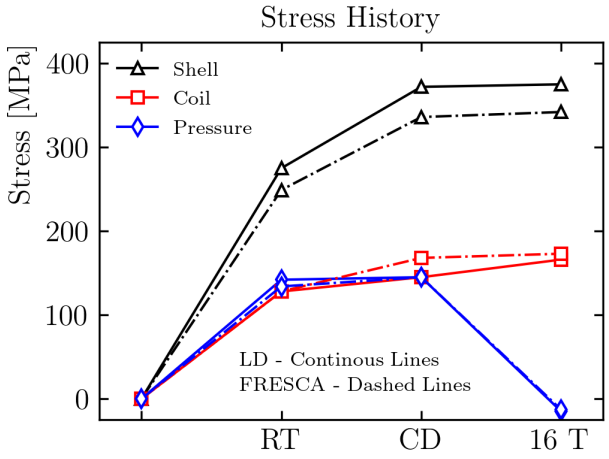

Fig. 8. Maximum Von Mises equivalent stress on the shell, the maximum equivalent stress on the coil and the contact pressure at the pole-coil interface during the magnet assembly, cooldown and powering to 16 T. The continuous lines show the results for the shifted coil layout, and the dashed lines for the aligned layout.

Fig. 6 shows the contact pressure/tension at this interface when the magnet reaches 16 T. The first regions to undergo tension are the upper corner of the inner coil, and the inner corner of the outer coil. The maximum tension, excluding the corner elements (0.5 mm wide), is equal to 15 MPa.

The Von Mises equivalent stress on the coil, during powering at 16 T, is shown in Fig. 7. The maximums stress is equal to 166 MPa, on the outer coil. This high stress region is relatively far from the aperture, in a region where the magnetic field is significantly lower. In the first two/three turns the stress is instead less than 78 MPa. Measurements of cables under transversal pressure suggest that at this stress level no critical current reduction should arise [21].

The evolution of the maximum equivalent stress on the shell and the coil is reported in Fig. 8. The plot also shows the pressure at the inner corner of the outer coil (the first to undergo unloading). Four points are shown: before loading, after loading at room temperature (RT), after cooldown at 1.9 K (CD), and during powering (16 T). The results are shown for the shifted and aligned coil layouts (see Fig. 2). The former allows for lower stresses in the coil after cooldown and during powering. The latter has a lower shell stress at every stage. The option with the lower coil stress seems preferable, as the shell stress can easily be reduced by increasing its thickness. Another option to allow higher stresses is to perform a more detailed analysis in the critical regions (Grade IV analysis, see [12]).

B. Coil Properties Sensitivity Analysis

A sensitivity analysis was performed to verify that the mechanical design meets the design targets within the range of uncertainties in the coil properties. For the design, an average value of 25 GPa and 3.8 mm were assumed merging the past experience from FRESCA2 [22] and MQXF [23]. However,

TABLE V
SENSITIVITY ANALYSIS RESULTS

Parameters	E_x	E_y	$\int \alpha_x dT$	$\int \alpha_y dT$
Unit	GPa	GPa	mm/m	mm/m
Nominal value	25	25	3.8	3.8
Range	15/35	25/45	2.9/4.7	2.9/3.8
Results				
Max. σ_{vm}, MPa	157/185	166/162	165/170	165/166
Max. $\lvert\sigma_x\rvert$, MPa	21/24	20/19	22/20	22/20
Δ Interference, µm	0/300	0/-150	-200/200	-100/0

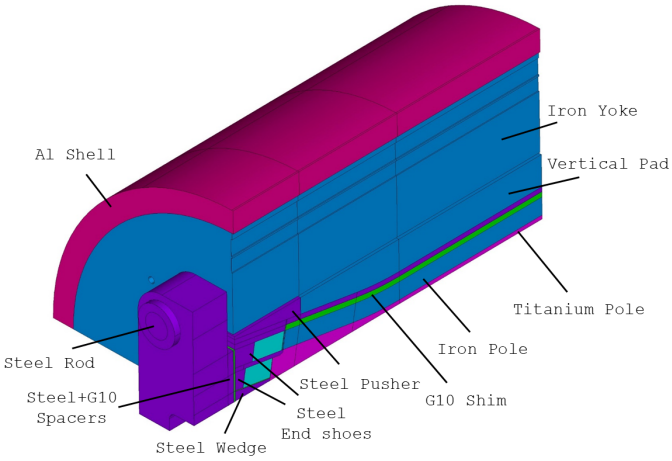

Fig. 9. 3D FE model of the TFD: the longitudinal prestress is provided by four longitudinal stainless steel rods.

measurements show that the coil properties can vary significantly even when the same cable is used [24]. An orthotropic variation of the vertical and horizontal Young's Moduli and thermal expansion coefficients was assumed, verifying the impact on the coil stress. In order to have comparable results, for each analysis the horizontal key interference was adjusted until the maximum tension criteria at the coil to pole interface was met.

The results from the analysis are shown in Table V, along with the values used for the various parameters. The magnet shows sufficient stability across the design space considered. Only a higher value of E_x leads to a non-negligible increase in stress. Increase in stress for this case is due to a less uniform tension profile ("spikes" near the coil corners) at the pole which requires an increase in key interference in order to meet the stringent maximum pole tension requirement.

C. 3D Mechanical Analysis

3D mechanical and magnetic models were developed to verify the magnet mechanical performances in the end region. The e.m. forces on the conductors were computed in OPERA, the reluctance forces in ANSYS, and the mechanical analysis was also performed in ANSYS. A view of the magnet FE model geometry is shown in Fig. 9: the longitudinal prestress is provided by stainless steel rods, connected to a steel plate that applies the prestress directly on the coil ends. The rods are stretched at room temperature by an hydraulic piston, and then locked in this deformed state with nuts. The model shows a further increase of the longitudinal prestress during cooldown:

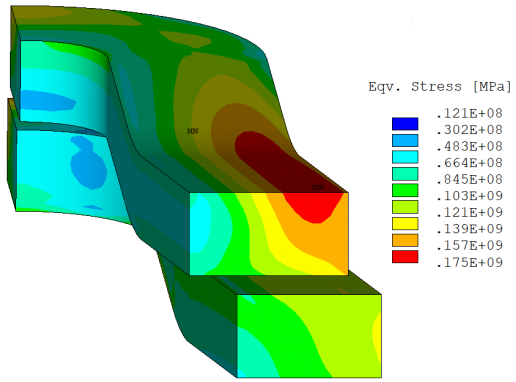

Fig. 10. Coil equivalent stress at 16 T, as computed with the 3D FE model.

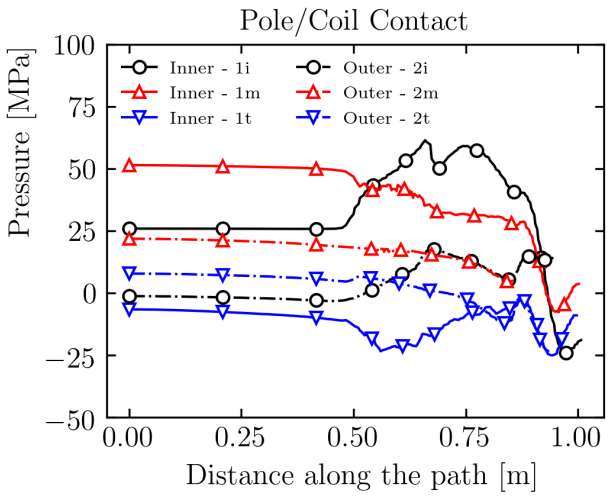

Fig. 11. Coil/pole contact pressure at 16 T on the inner and outer coil, at the inner (i), and top (t) edges, and in the middle (m).

the longitudinal contraction of the magnet is dominated by the iron yoke, which has a lower contraction with respect to stainless steel.

The computed stresses on the central cross-section of the magnet are consistent with what was obtained from the 2D models. However, the three-dimensional analysis showed that, to avoid unacceptable tension between the coil and the pole in the flared end region, an increase of horizontal prestress is necessary. The coil equivalent stress is slightly lower during loading (97 MPa), and higher after cooldown (179 MPa) and powering (175 MPa). The coil equivalent stress at 16 T is shown in Fig. 10.

Fig. 11 shows the contact pressure between the coil and the pole along the coil length. The maximum tension on the central cross-section of the magnet is located on the outer coil inner corner, and equal to 6 MPa. This is lower to what was found in the 2D analysis because of the horizontal prestress increase mentioned before. Approaching the ends, the tension increases, reaching a maximum of 25 MPa near the vertical symmetry plane (see Fig. 9). As this value does not satisfy the criteria proposed in Section III, the end region structure is undergoing a fine optimization.

VI. Conclusion

The paper analyzed the magnetic and mechanical design of the large aperture test facility dipole. A design criteria was introduced, which defines clear boundaries for the allowable stresses and contact conditions, and target parameters to consistently compare the performances of different designs.

At $1.9\,\mathrm{K}$, the magnetic design allows for a load line margin of 81.2% for a bore field of $16\,\mathrm{T}$. The peak magnetic field occurs in the inner coil and is equal to $16.5\,\mathrm{T}$.

The proposed design can satisfy the criteria with good margin: the maximum stress on the coil is kept below $166\,\mathrm{MPa}$, at $16\,\mathrm{T}$, within a $144\,\mathrm{mm}$ aperture and with a contact tension lower than $15\,\mathrm{MPa}$. Different design options were studied, and the shifted design was selected: this solution seems more efficient in keeping the coil stress low. The magnetic analysis suggests that this could be due to the lower force on the outer coil, which is in both cases the one that experiences the highest stresses. The analysis also showed that the design has low sensitivity to the coil properties: the only parameter able to generate a significant stress increase on the coil is its horizontal modulus.

References

[1] P. Bruzzone *et al.*, "Commissioning of the main coil of the EDIPO test facility," *IEEE Transactions on Applied Superconductivity*, vol. 24, no. 3, pp. 1–5, 2014, ISSN: 1558-2515. DOI: 10.1109/TASC.2013.2284721.

[2] G. Velev *et al.*, "Design and construction of a high field cable test facility at Fermilab," Proceedings of this conference, contribution ID: Wk2LPo3F.

[3] P. Ferracin *et al.*, "Mechanical design of HD2, a 15 T Nb_3Sn dipole magnet with a 35 mm bore," *IEEE Trans. Appl. Supercond.*, vol. 16, no. 2, p. 378, 2006.

[4] ——, "Development of the 15 T Nb_3Sn dipole HD2," *IEEE Trans. Appl. Supercond.*, vol. 18, no. 2, p. 277, 2008.

[5] P. Ferracin *et al.*, "Development of the EuCARD Nb_3Sn dipole magnet FRESCA2," *IEEE Transactions on Applied Superconductivity*, vol. 23, no. 3, pp. 4 002 005–4 002 005, Jun. 2013, ISSN: 1558-2515. DOI: 10.1109/TASC.2013.2243799.

[6] G. Willering *et al.*, "Tests of the FRESCA2 100 mm bore Nb_3Sn block-coil magnet to a record field of 14.6 T," *IEEE Transactions on Applied Superconductivity*, vol. 29, no. 5, pp. 1–6, 2019, ISSN: 1558-2515. DOI: 10.1109/TASC.2019.2907280.

[7] P. Ferracin *et al.*, "Design of LD1, a large-aperture high-field Nb_3Sn dipole magnet," *IEEE Transactions on Applied Superconductivity*, vol. 22, no. 3, pp. 4 901 604–4 901 604, Jun. 2012, ISSN: 1558-2515. DOI: 10.1109/TASC.2011.2179839.

[8] P. Bruzzone *et al.*, "Conceptual design of a large aperture dipole for testing of cables and insert coils at high field," *IEEE Transactions on Applied Superconductivity*, vol. 28, no. 3, pp. 1–5, Apr. 2018, ISSN: 1558-2515. DOI: 10.1109/TASC.2017.2785828.

[9] X. Sarasola *et al.*, "Magnetic and mechanical design of a 15 T large Aperture dipole magnet for cable testing," *IEEE Transactions on Applied Superconductivity*, vol. 29, no. 5, pp. 1–5, Aug. 2019, Conference Name: IEEE Transactions on Applied Superconductivity, ISSN: 1558-2515. DOI: 10.1109/TASC.2019.2896954.

[10] D. M. Araujo *et al.*, "Magnetic and mechanical 3-D modelling of a 15 T large aperture dipole magnet," *IEEE Transactions on Applied Superconductivity*, vol. 30, no. 4, pp. 1–5, Jun. 2020, ISSN: 1558-2515. DOI: 10.1109/TASC.2020.2969639.

[11] S. Caspi and P. Ferracin, "Limits of Nb_3Sn accelerator magnets," in *Proceedings of the 2005 Particle Accelerator Conference*, 2005, pp. 107–111. DOI: 10.1109/PAC.2005.1590372.

[12] S. Prestemon and E. Anderssen, "US HL-LHC accelerator upgrade project structural design criteria," *US-HILUMI-DOC-909*, 2018.

[13] H. Pan *et al.*, "Fracture failure analysis for MQXFA magnet aluminum shells," *IEEE Transactions on Applied Superconductivity*, vol. 30, no. 4, pp. 1–7, 2020, ISSN: 1558-2515. DOI: 10.1109/TASC.2020.2972230.

[14] I. A. Santillana and G. Vallone, "Characterization of low-carbon steel for high-field accelerator magnets," Unpublished.

[15] M. Reytier, F. Kircher, and B. Levesy, "Characterization of titanium alloys for cryogenic applications," *AIP Conference Proceedings*, vol. 614, no. 1, pp. 76–83, 2002, ISSN: 0094-243X. DOI: 10.1063/1.1472528.

[16] A. Devred, "Quench origins," in *AIP*, vol. 1262, 1992, pp. 1262–1308. DOI: 10.1063/1.41993. [Online]. Available: http://link.aip.org/link/APCPCS/v249/i2/p1262/s1%5C&Agg=doi.

[17] G. Vallone and P. Ferracin, "Modeling coil-pole debonding in Nb_3Sn superconducting magnets for particle accelerators," *IEEE Transactions on Applied Superconductivity*, vol. 27, no. 8, p. 4 004 611, 2017, ISSN: 1051-8223. DOI: 10.1109/TASC.2017.2759249.

[18] H. J. Hucek, K. E. Wilkes, K. R. Hanby, and J. K. Thompson, "Handbook on materials for superconducting machinery, includes data sheets for first and second supplements, November 1975 and January 1977," Battelle Columbus Labs, Ohio Metals and Ceramics Information Center, Tech. Rep., 1977.

[19] C. L. Goodzeit, "Superconducting accelerator magnets - an introduction to mechanical design and construction methods," *USPAS*, Jan. 2001.

[20] P. Ferracin *et al.*, "The HL-LHC low-β quadrupole magnet MQXF: From short models to long prototypes," *IEEE Transactions on Applied Superconductivity*, 2019.

[21] B. Bordini, P. Alknes, A. Ballarino, L. Bottura, and L. Oberli, "Critical current measurements of high-Jc Nb_3Sn rutherford cables under transverse compression," *IEEE Transactions on Applied Superconductivity*, vol. 24, no. 3, pp. 1–5, 2014, ISSN: 10518223. DOI: 10.1109/TASC.2013.2287309. [Online]. Available: http://ieeexplore.ieee.org/document/6648394/.

[22] E. Rochepault *et al.*, "Coil fabrication and assembly of the Nb_3Sn dipole magnet FRESCA2," *IEEE Transactions on Applied Superconductivity*, pp. 1–1, 2016, ISSN: 1051-8223. DOI: 10.1109/TASC.2016.2636145. [Online]. Available: http://ieeexplore.ieee.org/document/7775002/.

[23] G. Vallone *et al.*, "Mechanical performance of short models for MQXF, the Nb_3Sn low-beta quadrupole for the Hi-Lumi LHC," *IEEE Transactions on Applied Superconductivity*, pp. 1–1, 2016, ISSN: 1051-8223. DOI: 10.1109/TASC.2016.2645133. [Online]. Available: http://ieeexplore.ieee.org/document/7797180/.

[24] C. Fichera *et al.*, "New methodology to derive the mechanical behavior of epoxy-impregnated Nb_3Sn cables," *IEEE Transactions on Applied Superconductivity*, vol. 29, no. 7, p. 8 401 912, 2019, ISSN: 1051-8223. DOI: 10.1109/TASC.2019.2905224.